OPEN ACCESS

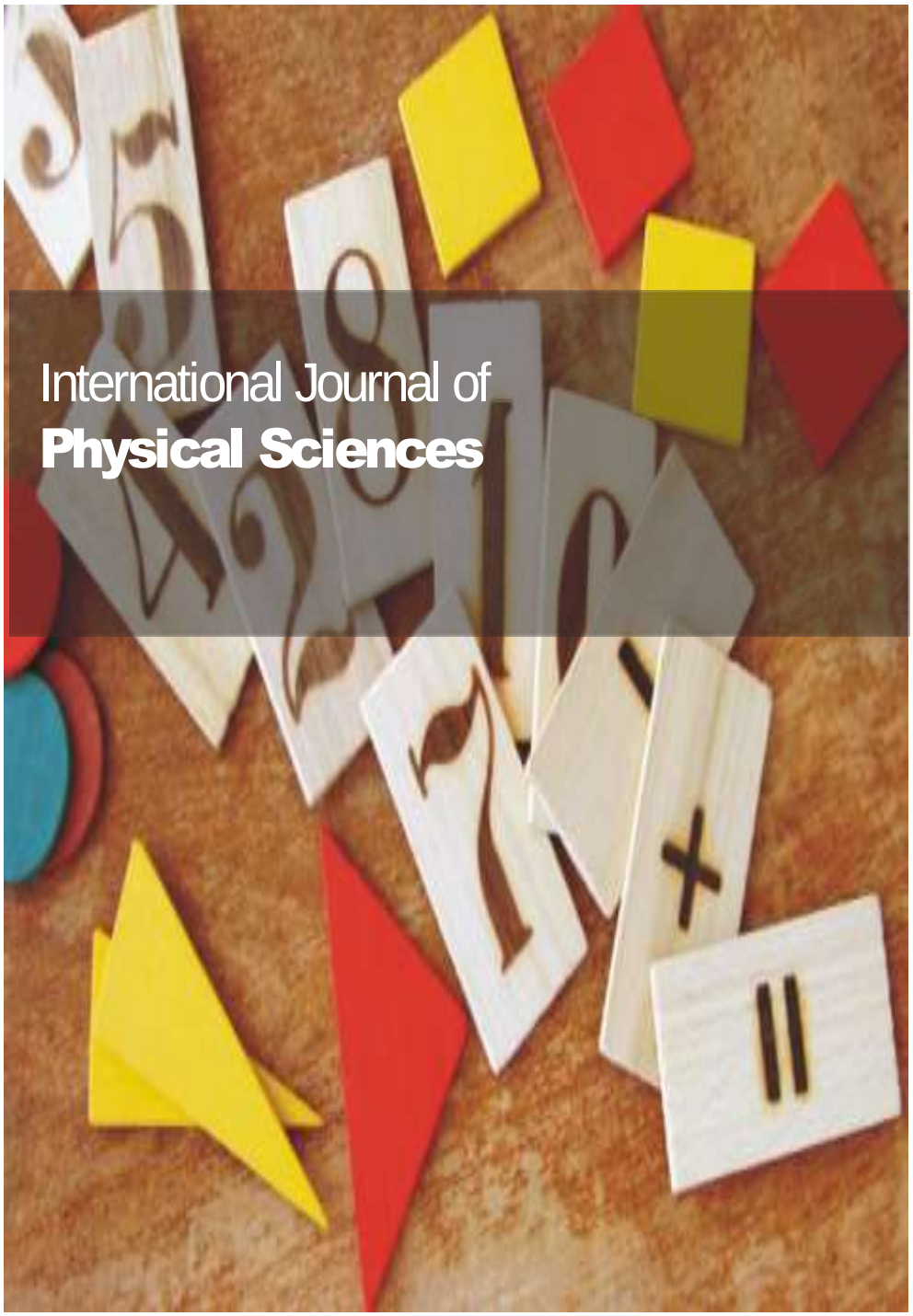

International Journal of Physical Sciences

30 December 2018
ISSN 1992-1950
DOI: 10.5897/IJPS
www.academicjournals.org

ACADEMIC JOURNALS
expand your knowledge

About IJPS

The International Journal of Physical Sciences (IJPS) is a peer reviewed journal. The journal publishes articles in all areas of physical sciences such as: Artificial intelligence, Neural processing, Nuclear and particle physics, Geophysics, Physics in medicine and biology, Plasma physics, Semiconductor science and technology Wireless and optical communications, Materials science, Energy and fuels, Environmental science and technology, Combinatorial chemistry, Geochemistry, Cement and concrete research, Metallurgy, Crystallography and Computer-aided materials design.

Open Access Policy

The International Journal of Physical Sciences is an Open Access journal. Abstracts and full texts of all articles published in this journal are freely accessible to everyone immediately after publication without any form of restriction.

Article License

All articles published by International Journal of Physical Sciences are licensed under the Creative Commons Attribution 4.0 International License. This permits anyone to copy, redistribute, remix, transmit and adapt the work provided the original work and source is appropriately cited. Citation should include the article DOI. The article license is displayed on the abstract page the following statement:

This article is published under the terms of the Creative Commons Attribution License 4.0
Please refer to https://creativecommons.org/licenses/by/4.0/legalcode for details
about Creative Commons Attribution License 4.0

Article Copyright

When an article is published by in the International Journal of Physical Sciences, the author(s) of the article retain the copyright of article. Author(s) may republish the article as part of a book or other materials. When reusing a published article, author(s) should;

Cite the original source of the publication when reusing the article. i.e. cite that the article was originally published in the International Journal of Physical Sciences. Include the article DOI
Accept that the article remains published by the International Journal of Physical Sciences (except in occasion of a retraction of the article)

Self-Archiving Policy

The International Journal of Physical Sciences is a RoMEO green journal. This permits authors to archive any version of their article they find most suitable, including the published version on their institutional repository and any other suitable website.
Please see http://www.sherpa.ac.uk/romeo/search.php?issn=1684-5315

Digital Archiving Policy

The International Journal of Physical Sciences is committed to the long-term preservation of its content. All articles published by the journal are preserved by Portico. In addition, the journal encourages authors to archive the published version of their articles on their institutional repositories and as well as other appropriate websites.
https://www.portico.org/publishers/ajournals/

Metadata Harvesting

The International Journal of Physical Sciences encourages metadata harvesting of all its content. The journals fully supports and implement the OAI version 2.0, which comes in a standard XML format. See Harvesting Parameter

Contact

Editorial Office: ijps@academicjournals.org

Help Desk: helpdesk@academicjournals.org

Website: http://www.academicjournals.org/journal/IJPS

Submit manuscript online http://ms.academicjournals.org

Academic Journals
73023 Victoria Island, Lagos, Nigeria
ICEA Building, 17th Floor,
Kenyatta Avenue, Nairobi, Kenya.

Editors

Editorial Board Members

Table of Content

Vol. 13(20), pp. 265-272, 30 December, 2018
DOI: 10.5897/IJPS2018.4763
Article Number: 3509A7659615
ISSN: 1992-1950

http://www.academicjournals.org/IJPS

International Journal of Physical Sciences

Full Length Research Paper

Assessment of outdoor radiation levels and radiological health hazards in Emene Industrial Layout of Enugu State, Nigeria

Ugbede F. O.[1*] and Benson I. D.[2]

[1]Radiation and Health Biophysics, Department of Physics with Electronics, Evangel University Akaeze, Ebonyi State, Nigeria.
[2]Department of Mathematics and Computer Science, Godfrey Okoye University, Enugu State, Nigeria.

Received 3 September, 2018; Accepted 3 December, 2018

A study to assess the outdoor Background Ionizing Radiation (BIR) levels in Emene Industrial Layout of Enugu State, Nigeria has been conducted. An *in-situ* measurement of BIR exposure rate in mRh^{-1} for 30 locations was done using a well calibrated portable GQ GMC-320 PLUS nuclear radiation detector at an elevation of 1.0 m above ground level with a geographical positioning system (GPS) for geographical location. The measured BIR exposure rates were used to evaluate the radiological health hazards and radiation effective doses to different body organs using well established radiological relations. The obtained values were compared with recommended permissible limits to ascertain the radiological health status of the environment. The mean values of BIR exposure levels (0.015 ± 0.001 mRh^{-1}), absorbed dose rates (126.15 ± 5.10 ηGyh^{-1}) and excess lifetime cancer risk ($0.541\pm0.032\times10^{-3}$) are higher than their recommended safe limits of 0.013 mRh^{-1}, 84.0 ηGyh^{-1}, 0.29×10^{-3} respectively as recommended by ICRP and UNSCEAR. The mean annual effective dose equivalent (0.155 ± 0.006 $mSvy^{-1}$) is within recommended permissible limits of 1.00 $mSvy^{-1}$ for general public exposure. Also, the effective doses to different body organs are all below the recommended limits of 1.0 $mSvy^{-1}$. Generally, the study shows that Emene Industrial Layout is radiologically contaminated due to industrial activities taking place. However, the contamination does not constitute any immediate radiological health effect on resident of the area but there is the potential for long-term health hazards in the future such as cancer due to accumulated doses.

Key words: BIR exposure level, effective dose, industrial activities, Emene Industrial Layout.

INTRODUCTION

The advent of industrialization coupled with poor environmental management systems have resulted to the release of various forms of toxic, corrosive and radioactive contaminants or pollutants into the environment. The negative health impact of industrial activities in the environment has been an issue of discussion in contemporary times. Environmental contamination and degradation is a global concern

*Corresponding author. E-mail: oghene4fred@yahoo.com; ugbedefred@evangeluniversity.edu.ng. Tel: +2348064148555.

because of its negative health impact. Background ionization radiation (BIR) could be considered as environmental contamination especially when it exceeds safe occupational and public limits (Agbalagba et al., 2016). BIR in the environment which was originally due to natural sources of terrestrial primordial radionuclides and extraterrestrial cosmic rays has over the years increased due to human activities and especially in the industrial environments. This is because raw materials used in industries contain naturally occurring radioactive materials (NORM) (Ademola and Olatunji, 2013) which are later released into the environment as waste after undergoing some industrial processes. Enhanced levels of naturally occurring radionuclides may be associated with certain natural materials, minerals and other resources used as raw materials in industries due to their region and origin (Lu and Zhang, 2006; Ademola and Olatunji, 2013). The most important are the series ^{238}U and ^{232}Th and their decay products as well as non series ^{40}K. Exploitation of these resources for the production of consumer items may lead to further enhancement of the radioactivity at concentrations above normal which are redistributed and released into the environment. The end result of this is increased BIR levels. This, in effect exposes the populace to high radiation doses and hazards.

Research data available on BIR levels assessment in some cities and towns worldwide show regions of low and high BIR levels. In Nigeria for example, Agbalagba et al. (2016) reported high radiation levels within Ughelli metropolis and its environs due to the industrial nature of the area. Agbalagba (2017) documented mean BIR exposure value of 0.022±0.006 mRh^{-1} in industrial zone of Warri city. James et al. (2013) studied the radiation levels of Idu industrial area of Abuja and recorded low radiation doses in the area. Akpabio et al. (2005) also studied the environmental radioactive levels in Ikot–Ekpene and reported that the radioactivity levels in the area is generally low ranging. Within Keffi and Akwanga towns of central Nigeria, Termizi-Ramli et al. (2014) also reported low radiation levels that are within recommended safe limits for the areas. Outside the country, Zarghani and Jafari (2017) recorded low range radiation doses in Birjand, Iran. In Chihuahua City, Mexico, Luevano-Gurrola et al. (2015) observed high outdoor gamma dose rates ranging from 113 to 310 ηGyh^{-1}.

High radiation levels and doses are detrimental to human health. Ionizing radiation are highly energetic particles with high penetrating power. When such radiation passes through a biological cell, it causes both excitation and ionization thereby altering the cells structure (Emelue et al., 2014). Exposure to high levels of gamma radiation causes a number of harmful effects in man such as mutation and cancer of various types (Aziz et al., 2014) and different kinds of diseases (Taskin et al., 2009). The practice of radiation protection has ensured that human exposure to radiation be kept to as low as reasonably achievable, called the ALARA principle (ICRP, 1973). One of the roles of radiation protection bodies is to ensure that the exposure of the public does not exceed certain safe limits as set up from time to time by regulatory agencies (Mokobia and Oyibo, 2017). Baseline data about BIR levels in Emene Industrial Layout (EIL) has not been established. Firstly, this study is aimed to report BIR exposure levels for the area and to assessing the impact of the industrial activities on BIR levels in the environment. The related radiological health indices are evaluated to know the health status of the environment.

MATERIALS AND METHODS

Study area

The study area, Emene Industrial Layout is located in Enugu East Local Government Area of Enugu State, South Eastern Nigerian. Thirty sampling points were carefully marked out for BIR exposure measurement which evenly covers the locations of the various industries/factories in the study area. Each of the sampling point was assigned a code (EIL1 to EIL30) for easy referencing. The nature of activities in the study area includes but not limited to the following; petroleum storage facilities, aluminum roofing sheet manufacturing, palm kernel oil extraction and processing, gas cylinders fabrication, gas storage and dispensing facilities, asphalt processing, saw mill, floor mill, plastic processing and production, metal fabrication/welding, automobile workshops and assembly plant, blocks/brick production, construction equipment yard, cement warehouses, asbestos production, oxygen and acetylene gases production, paint factory, etc.

Sampling and measurement

Measurement of terrestrial outdoor BIR exposure levels was done using a portable factory calibrated GQ GMC-320 PLUS nuclear radiation detector (from GQ Electronics LLC, USA). The radiation meter contains a Geiger-Muller detector tube capable of detecting α, β, γ and x-rays which was pre-set to detect background gamma radiation. The detector has a gamma energy range of 0.1 to 1.25 MeV and sensitivity of 0.1 ~ 1 MeV. When radiation passes through the Geiger tube, it triggers an electrical pulse for the CPU to register as a count in the basic count rate unit of Count per Minute (CPM). The CPM count rate indicates the radiation level and it can be converted to other traditional radiation units, such as mRh^{-1} or μSvh^{-1}. The working voltage of the detector is 3.6 to 3.7 V with power consumption rate of 25 to 125 mW dependent on the count rate.

The radiation level assessment was conducted for five months; from January to May 2018, with three BIR exposure readings taken for each sampling points at an interval of four minutes per month. This was done to account for any variation in the environmental parameters due to seasonal conditions (dry and wet seasons) and also to account for the fluctuating nature of radiation. The count rate per minute recorded in the detector was converted to radiation exposure in mRh^{-1} with an inbuilt converter according to Equation 1. A total of 15 measurements for each sample point were taken for the five months and the average recorded in this report as mean exposure readings. Readings were taken between the hours of 1300 and 1600 because the radiation meter has a maximum response to radiation within these hours as recommended by the

Table 1. BIR exposure levels and related radiological health indices in Emene Industrial Layout.

Sampling point code	Geographical location	Mean exposure reading (mRh^{-1})	Absorbed dose (ηGyh^{-1})	AEDE ($mSvy^{-1}$)	ELCR×10^{-3}
EIL1	N6º28'6.04" E7º36'4.76"	0.012	104.40	0.128	0.448
EIL2	N6º28'10.10" E7º36'10.47"	0.017	147.90	0.181	0.634
EIL3	N6º27'59.07" E7º35'47.69"	0.009	78.30	0.096	0.336
EIL4	N6º27'59.14" E7º35'44.74"	0.011	95.70	0.117	0.409
EIL5	N6º28'1.92" E7º35'58.74"	0.013	113.10	0.139	0.487
EIL6	N6º27'54.90" E7º35'34.54"	0.012	104.40	0.128	0.448
EIL7	N6º27'51.01" E7º35'24.69"	0.014	121.80	0.149	0.522
EIL8	N6º27'52.52" E7º35'25.49"	0.014	121.80	0.149	0.522
EIL9	N6º27'53.87" E7º35'28.95"	0.016	139.20	0.171	0.599
EIL10	N6º27'53.72" E7º35'31.56"	0.014	121.80	0.149	0.522
EIL11	N6º27'55.30" E7º35'40.30"	0.016	139.20	0.171	0.599
EIL12	N6º27'58.14" E7º35'37.61"	0.015	130.50	0.160	0.560
EIL13	N6º27'39.26" E7º34'45.88"	0.011	95.70	0.117	0.409
EIL14	N6º27'33.93" E7º34'42.06"	0.014	121.80	0.149	0.522
EIL15	N6º27'31.84" E7º34'46.82"	0.015	130.50	0.160	0.560
EIL16	N6º27'25.76" E7º34'41.86"	0.013	113.10	0.139	0.487
EIL17	N6º27'21.34" E7º34'52.07"	0.021	182.70	0.224	0.784
EIL18	N6º27'15.96" E7º34'44.01"	0.012	104.40	0.128	0.448
EIL19	N6º27'20.71" E7º34'2.25"	0.012	104.40	0.128	0.448
EIL20	N6º27'14.10" E7º34'4.79"	0.020	174.00	0.213	0.746
EIL21	N6º27'5.78" E7º34'6.41"	0.020	174.00	0.213	0.746
EIL22	N6º26'57.98" E7º34'4.82"	0.013	113.10	0.139	0.487
EIL23	N6º26'51.90" E7º34'6.83"	0.012	104.40	0.128	0.448
EIL24	N6º27'1.46" E7º34'11.45"	0.012	104.40	0.128	0.448
EIL25	N6º27'5.06" E7º34'20.53"	0.013	113.10	0.139	0.487
EIL26	N6º27'4.56" E7º34'27.36"	0.016	139.20	0.171	0.599
EIL27	N6º27'17.60" E7º33'56.14"	0.021	182.70	0.224	0.784
EIL28	N6º27'25.16" E7º34'31.43"	0.011	95.70	0.117	0.409
EIL29	N6º27'33.78" E7º34'36.13"	0.019	165.30	0.203	0.711
EIL30	N6º27'45.19" E7º35'3.08"	0.017	147.90	0.181	0.634
Mean value ±SED		0.015±0.001	126.15±5.10	0.155±0.006	0.541±0.032

National Council on Radiation Protection and Measurements (NCRP, 1993). An *in-situ* approach of measurement with the standard practice of raising the detector tube 1.0 m above ground level with its window facing the point under investigation was adopted to enable sample points maintain their original environmental characteristics (Agbalagba et al., 2016; Ugbede and Echeweozo, 2017). The precise locations of each of the sample point were determined using a geographical positioning system (GPS). The BIR exposure rate obtained were quantitatively used to assess the radiation health impact to the public in the immediate environments and radiation effective doses to different organs of the body by performing a number of radiological health hazard indices calculations using well established mathematical relations.

$$\text{Count rate per minute (CMP)} = 10^{-3}\, Roentgen \times Q.F \quad (1)$$

where Q.F is the quality factor, which is equal to 1 for external environments.

RESULTS AND DISCUSSION

The results for the BIR exposure level measurements and the related radiological health parameters are given in Table 1. Table 2 shows the results for the effective dose to some body organs. The different radiological health indices used in evaluating the radiation health status of the studied environment are absorbed dose, AEDE and the excess lifetime cancer risk (ELCR).

BIR exposure rate levels

The BIR exposure rate measured ranges from 0.009 to 0.021 mRh^{-1} with mean value of 0.015±0.001 mRh^{-1}. The mean exposure rate for the studied environment

Table 2. Dose to different organs of the body in Emene Industrial Layout.

Sampling point code	D_{organ} ($mSvy^{-1}$)						
	Lungs	Ovaries	Bone marrow	Testes	Kidney	Liver	Whole body
EIL1	0.082	0.074	0.088	0.105	0.079	0.059	0.087
EIL2	0.116	0.105	0.125	0.148	0.112	0.083	0.123
EIL3	0.061	0.056	0.066	0.079	0.060	0.044	0.065
EIL4	0.075	0.068	0.081	0.096	0.073	0.054	0.080
EIL5	0.089	0.081	0.096	0.114	0.086	0.064	0.095
EIL6	0.082	0.074	0.088	0.105	0.079	0.059	0.087
EIL7	0.095	0.086	0.103	0.122	0.092	0.069	0.101
EIL8	0.095	0.086	0.103	0.122	0.092	0.069	0.101
EIL9	0.109	0.099	0.118	0.140	0.106	0.079	0.116
EIL10	0.095	0.086	0.103	0.122	0.092	0.069	0.101
EIL11	0.109	0.099	0.118	0.140	0.106	0.079	0.116
EIL12	0.102	0.093	0.110	0.131	0.099	0.074	0.109
EIL13	0.075	0.068	0.081	0.096	0.073	0.054	0.080
EIL14	0.095	0.086	0.103	0.122	0.092	0.069	0.101
EIL15	0.102	0.093	0.110	0.131	0.099	0.074	0.109
EIL16	0.089	0.081	0.096	0.114	0.086	0.064	0.095
EIL17	0.143	0.130	0.155	0.184	0.139	0.103	0.152
EIL18	0.082	0.074	0.088	0.105	0.079	0.059	0.087
EIL19	0.082	0.074	0.088	0.105	0.079	0.059	0.087
EIL20	0.136	0.124	0.147	0.175	0.132	0.098	0.145
EIL21	0.136	0.124	0.147	0.175	0.132	0.098	0.145
EIL22	0.089	0.081	0.096	0.114	0.086	0.064	0.095
EIL23	0.082	0.074	0.088	0.105	0.079	0.059	0.087
EIL24	0.082	0.074	0.088	0.105	0.079	0.059	0.087
EIL25	0.089	0.081	0.096	0.114	0.086	0.064	0.095
EIL26	0.109	0.099	0.118	0.140	0.106	0.079	0.116
EIL27	0.143	0.130	0.155	0.184	0.139	0.103	0.152
EIL28	0.075	0.068	0.081	0.096	0.073	0.054	0.080
EIL29	0.130	0.118	0.140	0.166	0.126	0.094	0.138
EIL30	0.116	0.105	0.125	0.148	0.112	0.083	0.123
Mean value	0.099	0.090	0.107	0.127	0.096	0.071	0.105

exceeded the recommended permissible limit of 0.013 mRh^{-1} (ICRP, 2007; Osimobi et al., 2015; Agbalagba et al., 2016). The result indicates that 53.3% of the sample points exceeded the permissible BIR level for the general public. The variation and high exposure rate level is attributed to the different industrial activities carried out in the different sampling locations and their geophysical characterization. Petroleum products, chemicals and construction materials like asphalt, granites, cement, etc. have been recognized to contain some radioactive elements (Agbalagba et al., 2016) which enhance BIR level and are well available at the sample locations. The high BIR levels are suggestive indication that the environment is radiologically contaminated and unhealthy for the general public. The fluctuating pattern of the exposure level in comparison with recommended safe limit is shown in Figure 1. The mean exposure level reported here is lower than 0.018±0.004 mRh^{-1} value observed by Osimobi et al. (2015) in solid mineral mining sites of Enugu State, Nigeria. The mean value is higher than that measured by Ononugbo and Mgbemere (2016) in a fertilizer company in Onne, Rivers State, Nigeria which ranges between 11.73 and 14.95 ηRh^{-1}.

Absorbed dose rate (ADR) in air

The absorbed dose is used to assess the potential for any biochemical changes in specific tissues. It quantifies the radiation energy that might be absorbed by a potentially exposed individual. The measured BIR exposure levels were converted to radiation absorbed dose rate in air using Equation 2 according to Rafique et al. (2014) and Agbalagba (2017).

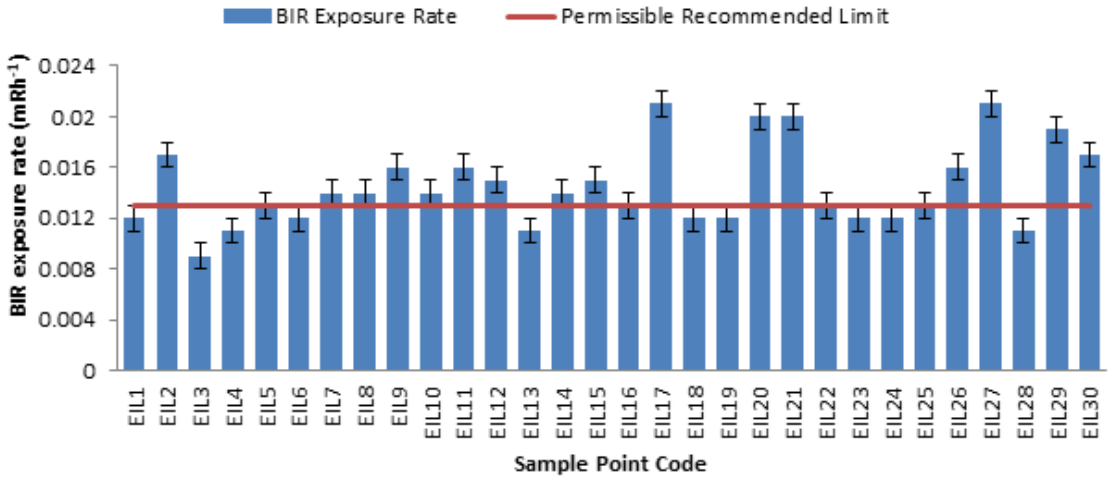

Figure 1. Comparison between BIR exposure rates in Emene Industrial Layout and permissible limit.

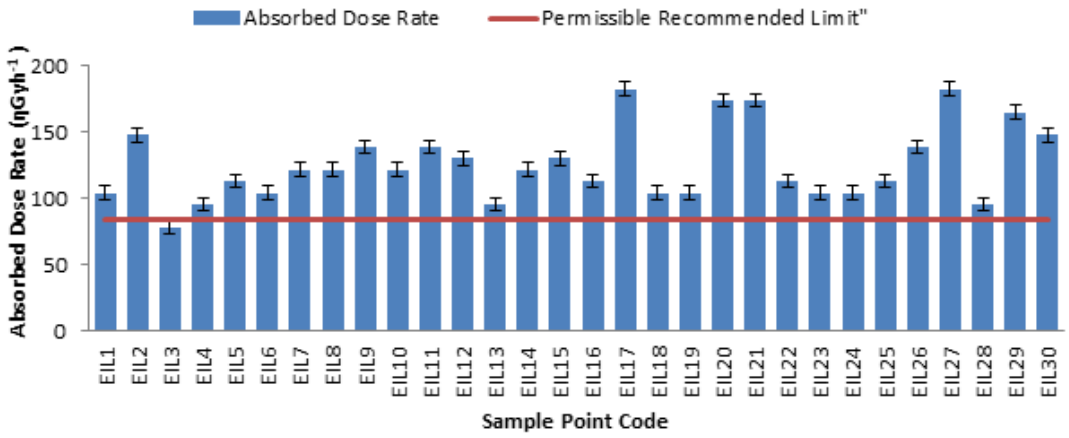

Figure 2. Comparison between the absorbed dose rate in Emene Industrial Layout and permissible safe limit.

$$1\mu Rh^{-1} = 8.7\eta Gyh^{-1} = \frac{8.7\times10^{-3}}{(1/8760y)}\mu Gyy^{-1} \quad (2)$$

This implies that:

$$1mRh^{-1} = 8.7\eta Gyh^{-1}\times10^{3} = 8700\eta Gyh^{-1} \quad (3)$$

The calculated absorbed dose rate ranges between 78.30 and 182.70 ηGyh^{-1} with observed mean value of 126.15±5.10 ηGyh^{-1}. These dose rates arising from BIR exposure in the studied locations are far higher than the recorded world weighted average of 59.00 ηGyh^{-1} (Agbalagba, 2017; Monica et al., 2016) and recommended safe limit of 84.0 ηGyh^{-1} (UNSCEAR, 2008; Ononugbo and Mgbemere, 2016) for outdoor exposure as shown in Figure 2. These dose rates show a radiation contaminated environment. Though the dose rate at these levels may not constitute any immediate health hazards to the residents of the locality, there is the potential for long-term health hazards in the future due to accumulated doses. The mean dose rate is higher than 97.44±20.42, 124.41±33.21, 97.44±12.17, 99.18±21.78 and 119.19±17.90 ηGyh^{-1} dose rates earlier reported by Benson and Ugbede (2018) in populated motor packs environment of Enugu city but lower than 141.30±31.31 ηGyh^{-1} for Warri city in Delta State, Nigeria reported by Agbalagba (2017) and 132.16±24.36 ηGyh^{-1} for Ughelli metropolis in Delta State Nigeria by Agbalagba et al. (2016).

Annual effective dose equivalent AEDE

The AEDE is used in radiation assessment and

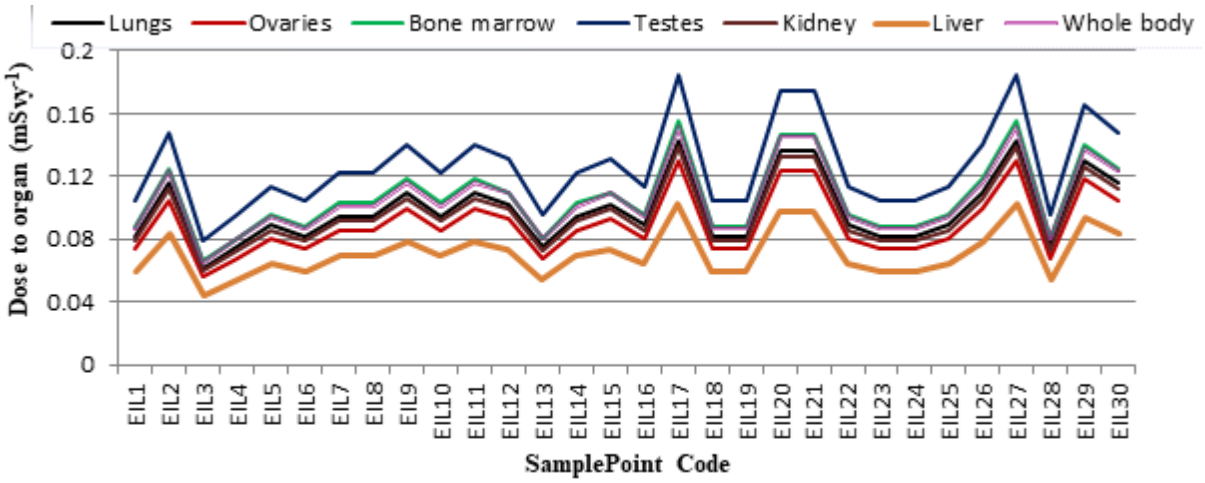

Figure 3. Comparison of the doses to different body organs.

protection to quantify the whole body absorbed dose per year. It is used to assess the potential for long-term effects that might occur in the future. The calculated absorbed dose rates were used to compute the AEDE within the study area using Equation 4 as given by Rafique et al. (2014) and Agbalagba (2017):

$$AEDE\left(mSvy^{-1}\right) = ADR\left(\eta Gyh^{-1}\right) \times 8760h \times 0.7\,Sv/Gy \times 0.2 \quad (4)$$

where ADR is the absorbed dose rate in ηGyh^{-1}, 8760 is the total hours in a year, 0.7Sv/Gy is the dose conversion factor from absorbed dose in air to the effective dose with an occupancy factor of 0.2 for outdoor exposure as recommended by UNSCEAR (2008).

The calculated values of AEDE range from 0.096 to 0.224 mSvy^{-1} with mean value of 0.155±0.006 mSvy^{-1}. This mean annual effective dose is higher than world average value of 0.07 mSvy^{-1} (ICRP, 2007; UNSCEAR, 2008; Agbalagba, 2017) but within ICRP and UNSCEAR recommended permissible limits of 1.00 mSvy^{-1} for the general public (ICRP, 2007; UNSCEAR, 2008). This implies that the studied location is radiologically contaminated due to the industrial activities taking place in the area. However, the contamination does not constitute any immediate radiological health effect on residents of the area. The annual effective doses evaluated in this study are similar to those reported by Ononugbo and Mgbemere (2016) in fertilizer producing area in Onne River State. The mean value is lower than 0.205±0.017 mean value observed in Idu industrial area of Abuja, Nigeria by James et al. (2013).

Effective dose to different body organs (D_{organ})

The effective dose to organs (D_{organ}) estimates the amount of radiation dose intake to various body organs and tissues. The D_{organ} of the body due to inhalation was calculated using Equation 5 as given by Darwish et al. (2015).

$$D_{organ}\left(mSvy^{-1}\right) = AEDE \times F \quad (5)$$

where F is the conversion factor of organ dose from air dose. The F value for lungs, ovaries, bone marrow, testes, kidney, liver and whole body as given by ICRP (1996) are 0.64, 0.58, 0.69, 0.82, 0.62, 0.46, and 0.68, respectively

The estimated average D_{organ} values for the lungs, ovaries, bone marrow, testes, kidney, liver and whole body due to radiation exposure and inhalation in the Emene industrial environment are 0.099, 0.090, 0.107, 0.127, 0.096, 0.071 and 0.105 mSvy^{-1} respectively. Figure 3 shows the variation of D_{organ} to the different organs. These results are all below the international tolerable limits of 1.0 mSv annually (Agbalagba, 2017) which further stress that the radiation levels do not constitute any immediate health effect on residents of the area. From the results, it is concluded that the testes and ovaries have highest and lowest sensitivity to radiation respectively. Similar conclusion has also been made by Darwish et al. (2015) and Agbalagba (2017).

Excess lifetime cancer risk ELCR

The ELCR was evaluated using the annual effective dose values using Equation 6 according to Rafique et al. (2014) and Agbalagba (2017)

$$ELCR = AEDE\left(mSvy^{-1}\right) \times DL \times RF \quad (6)$$

where DL is average duration of life (70 years) and RF is

the fatal cancer risk factor per sievert (Sv^{-1}). For low-dose background radiation, which is considered to produce stochastic effects, ICRP 103 uses a fatal cancer risk factor value of 0.05 for public exposure (ICRP, 2007).

The excess lifetime cancer risk is used in radiation protection assessment to predict the probability of an individual developing cancer over his lifetime due to low radiation dose exposure, if it will occur at all. The calculated values for the ELCR ranges from 0.336×10^{-3} to 0.784×10^{-3}. The mean ELCR value obtained is $(0.541 \pm 0.032)\times10^{-3}$. This mean value is approximately 86.6% higher than the world average value of 0.29×10^{-3}. This high value for excess lifetime cancer risk indicates that there exist the possibilities of cancer development by residents who wish to spend all their life time in the area. The ELCR values report here are lower than those reported by Agbalagba (2017) in industrial areas of Warri Nigeria and also lower than those for Okposi Okwu Salt Lake and Uburu Salt Lake environments of Ebonyi State, Nigeria reported by Avwiri et al. (2016).

Conclusion

This study so far has examined the radiological impact of industrial activities in Emene Industrial Layout by the assessment of the background radiation exposure levels in the area. From the study, the following conclusions are made:

1) The background radiation exposure rates shows that 53.3% of the sample locations indicate high radiation levels with mean value of 0.015±0.001 mRh^{-1} which is above 0.013 mRh^{-1} recommended limit for normal background radiation level.
2) The absorbed dose rates arising from BIR exposure are well above world average value which indicates a radiation contaminated environment.
3) The mean excess lifetime cancer risk value is 86.6% higher than the world average value. This suggests the possibility of cancer development in residents living in the area who wish to spend all their life time in the study area.
4) Generally, the study shows that Emene Industrial Layout is radiologically contaminated as a result of industrial activities taking place. The contamination and the radiation levels at these rates do not constitute any immediate health effect on residents of the area as shown by the effective dose to some organs of the body. However, there is the potential for long-term health hazards in future such as cancer due to accumulated doses.

RECOMMENDATIONS

1) The operators of the industries and concerned government agencies such as ministries of health and environment should devise means of reducing radioactive contaminants discharged into the environment to prevent further increase in the radiation level of the area.
2) High radioactive materials should be properly shielded and industries involved in the use of such materials be cited in isolated areas.
3) Residential buildings should be cited far away at places where the impact of the industries on BIR levels is less significant.
4) Regular monitoring of radiation levels in the area should be carried out by management of the various companies operating in the area, concerned government agencies and radiation protection scientists and agencies.
5) Further studies on radionuclides concentration in soil, water and crops planted in the area should be carried out.

CONFLICT OF INTERESTS

The authors have not declared any conflict of interests.

ACKNOWLEDGEMENTS

The authors thank Prof. C.E. Mokobia of Delta State University for releasing the radiation meter at subsidized rate as well as the managements of companies and residences of Emene Industrial Layout for giving free access to their compound.

REFERENCES

Ademola JA, Olatunji M A (2013). Evaluation of NORM and dose assessment in an aluminum industry in Nigeria. World Journal of Nuclear Science and Technology 3:150-154 http://dx.doi.org/10.4236/wjnst.2013.34025

Agbalagba EO, Avwiri GO, Ononugbo CP (2016). GIS mapping of impact of industrial activities on the terrestrial background ionizing radiation levels of Ughelli metropolis and its Environs, Nigeria. Environmental Earth Science 75:1425 DOI 10.1007/s12665-016-6216-y

Agbalagba OE (2017). Assessment of excess lifetime cancer risk from gamma radiation levels in Effurun and Warri city of Delta state, Nigeria. Journal of Taibah University for Science 11(3):367-380.

Akpabio LE, Etuk ES, Essian K (2005). Environmental radioactive levels in Ikot Ekpene Nigeria. Nigeria Journal of Space Research 1:80-87.

Avwiri GO, Nwaka BU, Ononugbo CP (2016). Radiological health risk due to gamma dose rates around Okposi Okwu and Uburu salt lakes, Ebonyi State. International Journal of Emerging Research in Management and Technology 5(9):36-46.

Aziz AQ, Shahina T, Kamal UD, Shahid M, Chiara C, Abdul W (2014). Evaluation of excessive lifetime cancer risk due to natural radioactivity in the rivers sediments of Northern Pakistan. Journal of Radiation Research and Applied Sciences 7:438-447.

Benson ID, Ugbede FO (2018). Measurement of background ionizing radiation and evaluation of lifetime cancer risk in highly populated motor parks in Enugu city, Nigeria. IOSR Journal of Applied Physics 10(3):77-82.

Darwish DAE, Abul-Nasr KTM, El-Khayatt AM (2015). The assessment

of natural radioactivity and its associated radiological hazards and dose parameters in granite samples from South Sinai, Egypt. Journal of Radiation Research and Applied Sciences 8:17-25

Emelue HU, Jibiri NN, Eke BC (2014). Excess lifetime cancer risk due to gamma radiation in and around Warri refining and petrochemical company in Niger Delta, Nigeria. British Journal of Medicine and Medical Research 4(13):2590-2598

International Commission on Radiological Protection (ICRP) (1973). International Commission on Radiological Protection Implication of Commission Recommendations 22 that doses be kept As Low as Reasonably Achievable (ALARA).

International Commission on Radiological Protection (ICRP) (1996). International Commission on Radiological Protection Age-dependent Doses to Members of the Public from Intake of Radionuclides. Part5: Compilation of Ingestion and Inhalation Coefficients ICRP Publication 72, Pergamon Press, Oxford.

International Commission on Radiological Protection (ICRP) (2007). The 2007 Recommendations of the International Commission on Radiological Protection: Annals of the ICRP Publication Elsevier. 103:2-4.

James IU, Moses IF, Vandi JN (2013). Assessment of gamma dose rate within Idu industrial area of the Federal Capital Territory (FCT) Abuja, Nigeria. The International Journal of Engineering and Science 2(11):52-55.

Lu XW, Zhang XL (2006). Measurement of natural radioactivity in sand samples collected from Baoji Weihe sands park, China. Environmental Geology 50(7):977-982. http://dx.doi.org/10.1007/s00254-006-0266-5

Luevano-Gurrola S, Perez-Tapia A, Pinedo-Alvarez C, Carrillo-Flores J, Montero-Cabrera ME, Renteria-Villalobos M (2015). Lifetime effective dose assessment based on background outdoor gamma exposure in Chihuahua City, Mexico. International Journal of Environmental Research and Public Health 12:12324-12339. doi:10.3390/ijerph121012324

Mokobia CE, Oyibo B (2017). Determination of background ionization radiation (BIR) levels in some selected farms in Delta State, Nigeria. Nigerian Journal of Science and Environment 15(1):27-31.

Monica S, Visnu Prasad AK, Soniya SR, Jojo PJ (2016). Estimation of indoor and outdoor effective doses and lifetime cancer risk from gamma dose rates along the coastal regions of Kollam district, Kerala. Radiation Protection and Environment 39(1):38-43.

National Council on Radiation Protection (NCRP) (1993). National Council on Radiation Protection and Measurements: Limitation of exposure to ionizing radiation, NCRP report No.116.

Ononugbo CP, Mgbemere CJ (2016). Dose rate and annual effective dose assessment of terrestrial gamma radiation in Notre fertilizer plant, Onne, Rivers State, Nigeria. International Journal of Emerging Research in Management and Technology 5(9):30-35

Osimobi JC, Agbalagba EO, Avwiri GO, Ononugbo CP (2015). GIS mapping and background ionizing radiation (BIR) assessment of solid mineral mining sites in Enugu State, Nigeria. Open Access Library Journal 2:1-9. http://dx.doi.org/10.4236/oalib.1101979

Rafique M, Saeed UR, Muhammad B, Wajid A, Iftikhar A, Khursheed AL, Khalil AM (2014). Evaluation of excess life time cancer risk from gamma dose rates in Jhelum valley. Journal of Radiation Research and Applied Sciences 7:29-35

Taskin H, Karavus M, Ay P, Topuzoglu A, Hindiroglu S, Karahan G (2009). Radionuclide concentrations in soil and lifetime cancer risk due to the gamma radioactivity in Kirklareli. Turkey Journal of Environmental Radioactivity 100:49-53.

Termizi-Ramli A, Aliyu AS, Agba EH, Saleh MA (2014). Effective dose from natural background radiation in Keffi and Akwanga towns, central Nigeria. International Journal of Radiation Research 12(1):47-52.

Ugbede FO, Echeweozo EO (2017). Estimation of annual effective dose and excess lifetime cancer risk from background ionizing radiation levels within and around quarry site in Okpoto-Ezillo, Ebonyi State, Nigeria. Journal of Environment and Earth Science 7(12):74-79

United Nations Scientific Committee on the effect of Atomic Radiation (UNSCEAR) (2008). Report on the sources and effects of ionizing radiation. Report to the General Assembly with Scientific Annexes. United Nations, New York.

Zarghani H, Jafari R (2017). Assessment of outdoor and indoor background gamma radiation, the annual effective dose and excess lifetime cancer risk in Birjand, Iran. Jundishapur Journal of Health Sciences 9(3):1-4. doi: 10.17795/jjhs-40791.

Vol. 13(20), pp. 273-281, 30 December, 2018
DOI: 10.5897/IJPS2018.4759
Article Number: 734017459617
ISSN: 1992-1950

http://www.academicjournals.org/IJPS

International Journal of Physical Sciences

Full Length Research Paper

Magnetosphere convection electric field (MCEF) time variation from 1964 to 2009: Investigation on the signatures of the geoeffectiveness coronal mass ejections

Kaboré Salfo and Ouattara Frédéric*

Laboratoire de Recherche en Energétique et Météorologie de l'Espace (LAREME), Université Norbert Zongo (Anciennement Université de Koudougou), BP 376 Koudougou Burkina Faso.

Received 22 August, 2018; Accepted 27 November, 2018

The signatures of the geoeffectiveness solar disturbed events on the Magnetosphere Convection Electric Field (MCEF) universal time variation from 1964 to 2009 are investigated. Here, attention is focused our on the periods concerned by the whole shock activity and by the different types of the geoeffectiveness Coronal Mass Ejections (CMEs) which are one-day-shock, two-days-shock and three-days-shock. The investigation is made with respect to the orientation of the Interplanetary Magnetic Field (IMF). The MCEF time profiles show three different trends except for one-day-shock activity and for three-days-shock activity where we have four trends and one trend, respectively. The MCEF time profiles of the whole disturbed activity, the all shock activity and the one-day-shock activity present the initial phase where the Interplanetary Magnetic Field (IMF) is southward. During the two-days-shock activity, the initial phase of the MCEF shows a non-sensitive trend to the change of the direction of the IMF z-component while for the three-days-shock activity, the MCEF always exhibits the signature of the northward IMF. The last trend of the MCEF time profile shows the southward IMF signature except for the one-day-shock and the three-days-shock activities where that of the northward IMF was seen.

Key words: Magnetosphere convection electric field, interplanetary magnetic field, shock activity, coronal mass ejections (CMEs).

INTRODUCTION

The magnetosphere created by the solar wind is a very sensitive and dynamic entity (Russel, 1979) a behaviour that depends on the properties of the solar wind plasma and its frozen magnetic field (Mc Pherron et al., 2007). According to Mc Pherron et al. (2007), there are three possible magnetic topologies during the interaction between the solar wind and the planetary magnetosphere. Among them, we can cite the topology where a magnetic line might not intersect the Earth at all and that where a magnetic line might intersect the surface of the Earth

*Corresponding author. E-mail: fojals@yahoo.fr.

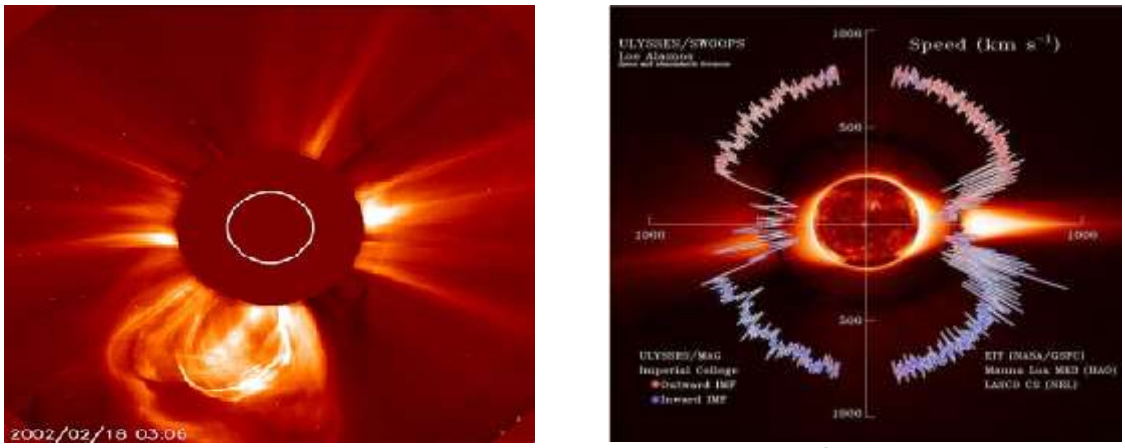

a b

Figure 1. Solar disturbance events. The panel a concerns high speed solar wind stream coming from coronal holes, slow solar wind stream coming from the neutral sheet and the CMEs. The panel b shows the two type of wind speed as measured by ULYSSE with the outward IMF (in red) and inward IMF (in blue).

twice (Russel, 2007). During the topology where there is an interaction between the solar wind and the planetary magnetosphere, two mechanisms are invoked to explain such interaction. The first one concerns the mechanism of Axford and Hines (1961), namely the viscous interaction (always present) where closed magnetic flux tubes are transported from the dayside to nightside. The second mechanism is that of Dungey (1961), namely magnetism reconnection. In that case, Russell (1979) notes that when the interplanetary magnetic field (IMF) is southward, its field lines convect along the solar wind break in half and join partners with magnetospheric lines and when the IMF is northward, the reconnection cannot take place at the nose of the magnetosphere but there are other places where antiparallel fields occur and it might take place.

It is known that there are two approaches to magnetospheric studies (Russel, 1979): (1) the statistical approach in which one thing is examined many times and (2) the case history approach in which one or two examples are looking very carefully. The present work concerns the first approach.

Several authors (Legrand and Simon, 1989; Richardson et al;, 2000; Richardson and Cane, 2002; Ouattara and Amory Mazaudier, 2009) showed that the geomagnetic storms [defined as global magnetic disturbances that result from the interaction between magnetized plasma propagating from the Sun and magnetic fields in the near-Earth space environment (Tommaso et al., 2016)] can be due to (1) recurrent activity (due to solar high stream wind coming from coronal holes), (2) shock activity (produced by the geoeffectiveness CMEs) and (3) fluctuating activity (caused by the geoeffectiveness fluctuating solar wind provoked by the fluctuation of solar neutral sheet) (Figure 1).

It is well known that the state of the Earth magnetosphere depends on the orientation of the IMF z-component (namely B_z and perpendicular to the ecliptic plan) during solar Wind-Earth magnetosphere interactions or CMEs-Earth magnetosphere interactions. Here we are concerned with the statistical behaviour of the Magnetosphere Convection Electric Field (MCEF) time variation (Universal Time: UT) under the action of the geoeffectiveness CMEs with respect to orientation of the IMF z-component. As shown by Gyébré et al. (2015), the shock activity due to the geoeffectiveness CMEs action can be divided into three types with respect to their time duration (one-day-shock, two-days-shock and the three-days-shock; detail on this typology is subsequently given as the present paper deals with each type of shock action on the Earth MCEF by taking into account the orientation of the IMF z-component.

For evaluating the different solar events impact on the Earth magnetosphere and specifically that of the three types of shock activity in the Earth MCEF, in our study we follow the method of Legrand and Simon (1989) that consists of using a pixel diagram for getting the overview of the yearly geoeffectiveness solar events; this overview can be extended to the whole period involved with given a continuum of several pixel diagrams. It is important to underline that this method does not require the knowledge of solar wind parameters for selecting each type of solar events (quiet or each type of disturbed events). This is in view of the fact that this method has been developing before having all solar wind parameters through satellites data (year 1989) and has been validated by Ouattara and Amory Mazaudier (2009). Therefore, pixel diagram appears as a good tool because its gives an excellent result during the evaluation of geomagnetic storms effects on ionosphere (e.g. Gyébré et al., 2018 and the reference therein about the use of the pixel diagrams). Thus, it is now clear that our objective is not to determine the different solar geoeffectiveness events by using the characteristic of the solar wind

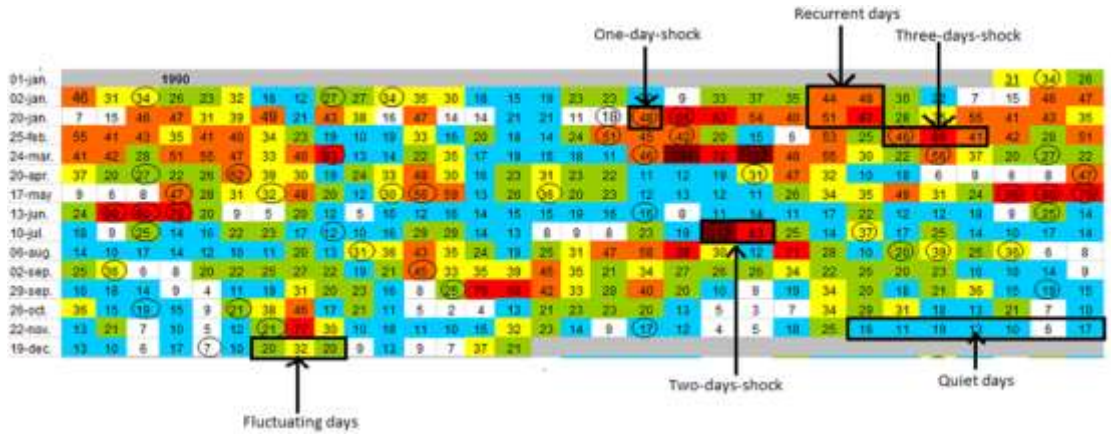

Figure 2. Pixel diagram of the year 1990 where are highlighted the four geomagnetic days with each type of shock activity.

parameters (that is already done by a pixel diagram) but to understand and to analyse each geoeffectiveness solar event (identifying by a pixel diagram) impact on the Earth's magnetosphere. This will be done with respect to the orientation of the IMF z-component.

In the present paper, we focus our attention on the impacts of the geoeffectiveness CMEs. The other geoeffectiveness disturbed events impacts will be analysed in our coming papers. The novelty of the present investigation is based on the consideration of the different types of shock activity.

Before analysing the Universal Time (UT) variability of the Earth MCEF (E_M) [that is, the electric field imposed on the magnetosphere by the solar wind interaction] under the shock conditions, we firstly analyse its UT variation during quiet periods and secondly during the whole disturbed periods (periods due to recurrent, fluctuating and shock activities) in order to appreciate the impact of the whole disturbed conditions on UT variation of the Earth MCEF with respect to that of the quiet time. After analysing the UT variation of the Earth MCEF under the shock conditions, we focus our attention on the UT variation of the Earth MCEF during each type of the shock activity.

MATERIALS AND METHODS

For studying the UT variation of the Earth MCEF under the shock activity, several parameters are used: (1) the Mayaud (1971, 1972) geomagnetic index aa, (2) the sudden storm commencement (SSC) dates and (3) the y-component (namely Ey) of the solar wind motion electric field (SWEF) and expressed by $E_y = V.B_z$ where V is solar wind velocity and B_z the interplanetary magnetic field intensity in the direction perpendicular to the ecliptic plane.

Method for determining the shock activity

The shock activity days are determined by means of the pixel diagrams (Figure 1) carried out by using the aa daily values (Ouattara and Amory Mazaudier, 2009). These diagrams highlight the repartition of the geomagnetic data as a function of the solar activity as described by solar rotation (27 days) (Ouattara and Amory Mazaudier, 2009; Gyébré et al., 2015). The four geomagnetic classes of activity [(1) quiet activity due to the slow solar wind, (2) recurrent activity caused by the high stream solar wind, (3) fluctuating activity provoked by the fluctuating solar wind and (4) shock activity that results from the action of the geoeffectiveness CMEs (Coronal Mass Ejections)] as defined by Legrand and Simon (1989), Simon and Legrand (1989), Richardson et al. (2000) and Richardson and Cane (2002). Gyébré et al. (2015) divided the shock activity into three types according to their time duration (one day, two days and three days): (1) one-day-shock, (2) two-days-shock and (3) three-days-shock activities. The one-day-shock corresponds to only a day when SSC occurs whatever its arrival time; the two-days-shock is shown by the SSC day with a day after this day (the concerning two days are the total days where this shock effects are seen) and the three-days-shock is identified by the SSC day with two days after this day (the involved three days are the total days where this shock effects are observed) (Gyébré et al., 2015, 2018). A pixel diagram (Figure 2) shows the three types of shock activity.

For the specific period, the whole pixel diagrams exhibit 323 shock-days with 168 days of one-day-shock, 105 days of two-days-shock and 50 days of three-days-shock (Gyébré et al., 2015).

Method for determining the magnetospheric convection electric field

Because our investigation period involved several years before the availability of the overall measurements of the solar wind parameters, the UT variation of the MCEF (E_M) will be computed by using the linear correlation between the hourly data of the SWEF (E_y) and that of the MCEF established by Revah and Bauer (1982) and given by the following equation: $E_M = 0.13\,E_y + 0.09$. In this equation, the correlation coefficient (r) value is 0.97. The hourly values of the SWEF are taken from OMNIWEB web site: *http://omniweb.gsfc.nasa.gov/form/dx1.html* whereas those of the MCEF are computed through the above equation and for the period 1964-2009 (this period corresponds to the four solar cycles involved). It is important to note that each hourly E_M value is computed by using the hourly arithmetic mean values of the E_y

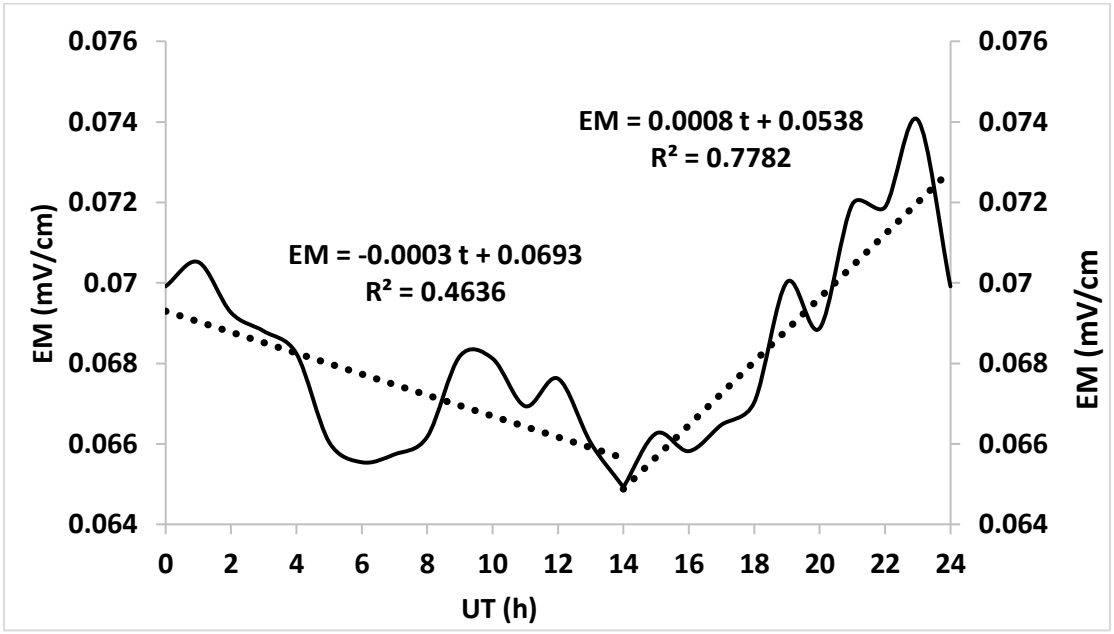

Figure 3. Magnetosphere convection electric field UT variation for quiet-days activity.

values of the concerning events for the period involved.

RESULTS AND DISCUSSION

Figure 3 shows the daytime variability of the MCEF during the quiet period. The linear curves are obtained by the least squares method. It can be seen that the MCEF graph highlights a decreasing phase from 0000 UT to 1400 UT and an increasing phase from 1400 UT to 24000 UT. The decreasing trend slope is $-\frac{3\ 10^{-4}mV}{cm.s}$ with correlation coefficient 0.609 and that of the increasing trend is $+\frac{8\ 10^{-4}mV}{cm.s}$ with correlation coefficient value 0.8822.

According to McPherron et al. (2007), a geomagnetically quiet time can be identified on one hand by the absence of the reconnection between the IMF and the geomagnetic field. During that case, tangential stress is applied by means of viscous interaction that transports closed magnetic flux tubes from the dayside to the night side (Axford and Hines, 1961); and on the other hand, by the reconnection between the northward IMF and the geomagnetic field. Croker (1992) noted that this reconnection connects in the tail lobes open lines to IMF lines and does not induce change in the amount of lobe flux. The analysis of the Figure 3 enable the assertion according to the model of Axford and Hines (1961) that the decreasing phase of the CMEF corresponds to the lack of closed magnetic flux tubes and its increasing phase pointed out the accumulation of the flux tubes by the viscous interaction. It may also be due to the reconnection in the tail lobes after the dayside reconnection between the geomagnetic field line and that of the northward IMF. The MCEF increases until the magnetosphere returns to a nominal condition characterized by its initial value. This is exhibited by the decreasing of the MCEF intensity from 2300 UT to 2400 UT.

The two different trends of the MCEF shows two different states of the magnetosphere: the first one characterized the period (0000 UT -1400 UT) of the viscous interaction where closed magnetic flux are transported tail ward and the second one corresponds to the period (1400 UT -2400 UT) of the reconnection in the tail lobes with the northward IMF. This result points out that 1400 UT is the time of the change of the state of the magnetosphere from viscous interaction and northward IMF interaction. The MCEF values oscillate between 0.0651 mV/cm (before 1400 UT) and 0.0426 mV/cm (after 1400 UT).

Figure 4 concerns the variability of the MCEF during the whole disturbed activity. One can see the increasing phase from 0000 UT to 1600 UT with increasing trend slope value of $\frac{3\ 10^{-4}mV}{cm.s}$ with 0.5857 as the correlation coefficient value and the decreasing phase from 1600 UT to 2100 UT with the decreasing slope value - $\frac{2.1\ 10^{-3}mV}{cm.s}$ with the correlation coefficient value of 0.9504. It appears as a night time increasing phase (from 2100 UT to 2400 UT) with $\frac{3.5\ 10^{-3}mV}{cm.s}$ as the trend slope value and the correlation coefficient value of 0.8557.

From 0000 UT to 1400 UT and from 1400 UT to 2100

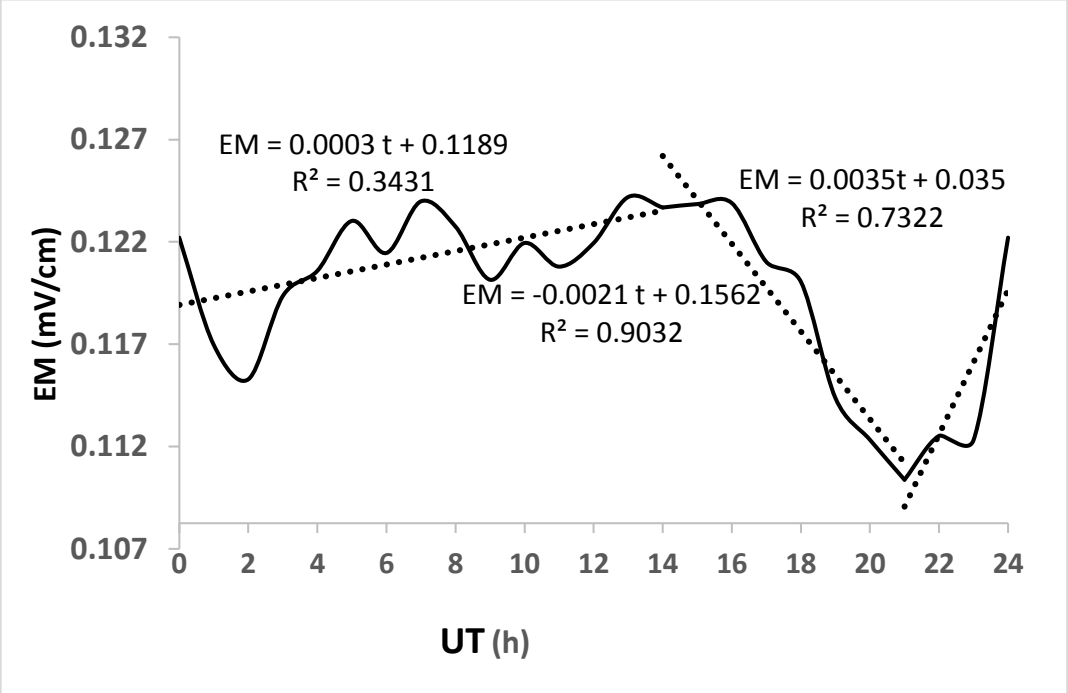

Figure 4. The same as Figure 3 but for the whole disturbed activity.

UT, the variability of MCEF for quiet time and that of disturbed period vary in opposite phase.

During disturbed time, the daily values of MCEF vary from 0.1100 to 0.1245 mV/cm with 0.1194 mV/cm as the daily mean value, while during quiet time, the MCEF varies from 0.06492 to 0.0720 mV/cm with daily mean value of 0.0676 mV/cm.

Figure 4 shows the time variation of MCEF during the geomagnetic storm conditions. In that case, there was a reconnection between the geomagnetic field line and that of the southward IMF (Dungey, 1961). It can be interpreted as the change of the IMF from northward (quiet condition) to southward (disturbed condition). Nishimura et al. (2009) noted that the MCEF reacts to this change and de Siqueira et al. (2011) underlines that the MCEF increases after the change of the IMF from northward to southward. Therefore, the increasing phase of the MCEF corresponds to the sustained southward IMF and consequently shows the storm main phase (Partamies et al., 2011). The beginning of this phase corresponds to the onset time of the change of the IMF from northward to southward. As this change implies the intensification of the ring current (Mannucci et al., 2008; Nishimura et al., 2009) and the geomagnetic storm is identified by the intensification of the ring current (Gonzalez et al., 1994), one can conclude that the increasing phase of the MCEF expressed the phase where geomagnetic activity increases. The decreasing phase which occurs after the increasing phase shows the phase of the change of the IMF from southward to northward. In fact, according to Kelley et al. (1979), the magnetospheric convection is weakened when the IMF turns from southward to northward. The following increasing phase may be due to the night side reconnection.

The analysis of the Figure 3 enables three phases: (1) the dayside reconnection with southward IMF, (2) the period (1600 UT -2100 UT) where the IMF changes from southward to northward and maintains northward until 2100 UT, and (3) the night side reconnection.

Figure 4 is devoted to the time variation of MCEF for the overall shock activity. The MCEF increases from 0000 UT to 1200 UT with the slope value of $\frac{2.3\ 10^{-3}mV}{cm.s}$ and 0.7115 as the correlation coefficient value. Between 1200 UT to 1500 UT, the MCEF decreases with - $\frac{2.27\ 10^{-2}mV}{cm.s}$ as its trend slope value with the correlation coefficient value of 0.9949. After 1500 UT until 2400 UT, we observe an increasing phase with $\frac{6.6\ 10^{-3}mV}{cm.s}$ as the trend slope and the correlation coefficient value of 0.8642.

When the MCEF acts, the overall shock activity varies from the minimum value of 0.137 mV/cm and the maximum value of 0.217 mV/cm with a mean value of 0.183 mV/cm.

In this case, the geomagnetic activities are considered due to the geoeffectiveness coronal mass ejections (CMEs). Figure 5 graph shows the same time variation as that of the Figure 4 except that the former (first and second) phases of the overall shock activity are shorter than that of the whole disturbed activity.

It can be retained from this figure that there are three

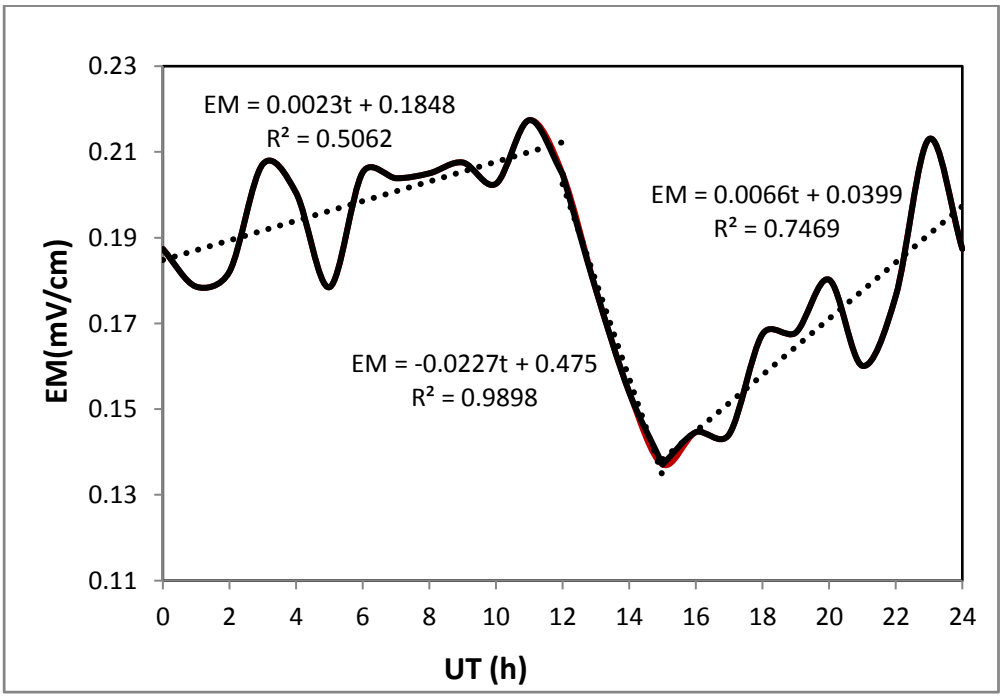

Figure 5. The same as figure 3 but for the all shock activity.

phases per day for the state of the magnetosphere. The first one corresponds to the period of change of the IMF from the northward to the southward and this direction is maintained until 1200 UT. The second phase begins by the change of the IMF from southward to northward and maintains this direction until 1400 UT. The third phase highlights the period of the reconnection at night time.

The comparison between the beginning time of the different phase of the state of the magnetosphere shows that it is better to target each type of disturbed activity instead of investigating the different disturbed activities as a whole disturbed activity.

Figure 6 concerns the MCEF diurnal variation for one-day-shock activity. During this activity, the MCEF exhibits four trends. It emerges from this figure that the MCEF increases from 0000 UT to 1200 UT. The trend slope and the correlation values are $\frac{6.5\ 10^{-3}mV}{cm.s}$ and 0.86, respectively. Between 1200 UT and 1500 UT the MCEF decreases with the trend slope value of - $\frac{2.7\ 10^{-2}mV}{cm.s}$ and the correlation coefficient value of 0.9173. From 1500 UT to 1900 UT we have an increasing phase with the trend slope and the correlation values of $\frac{2.7\ 10^{-2}mV}{cm.s}$ and 0.9173, respectively. After this increase, the MCEF decreases from 1500 UT to 2400 UT. The trend slope for this phase is - $\frac{6.8\ 10^{-3}mV}{cm.s}$ with the correlation coefficient of 0.7495.

The MCEF of the one-day-shock activity varies from the minimum (0.038 mV/cm) to the maximum (0.168 mV/cm) with a mean value of 0.132 mV/cm.

The MCEF of the one-day-shock activity presents four phases: two increasing phases and two decreasing phases. Each increasing phase is followed by a decreasing phase. This let us assert that the IMF turns four times when it acts on the one-day-shock. The latest phase of the overall shock activity corresponds to southward IMF (Figure 5) and that of the one-day-shock shows the signature of the northward IMF (Figure 6).

Analysis of the Figure 6 shows that there is no night side reconnection because the MCEF end the day by its decreasing phase. This is an important result because on one hand, one-day-shock activity impact differs from that of the whole shock activity and on the other hand, the night side reconnection does not occur at all time after the disrobed period.

Figure 7 highlights the time variation of the MCEF during the action of the two-days-shock. From 0000 UT to 1000 UT, the MCEF is fairly constant where its values oscillated between 0.26 mV/cm and 0.225 mV/cm. Between 1000 UT and 1600 UT, the MCEF shows decreasing phase with a slope of - $\frac{1.36\ 10^{-2}mV}{cm.s}$ with the correlation coefficient value of 0.9458. After that, we see an increasing phase from 1600 UT to 2400 UT. The slope of this phase is - $\frac{1.31\ 10^{-2}mV}{cm.s}$ with 0.8788 as correlation coefficient value.

The mean value of the MCEF is 0.229 mV/cm with the minimum value of 0.158 mV/cm and the maximum value of 0.281 mV/cm.

During two-days-shock activity, the magnetosphere

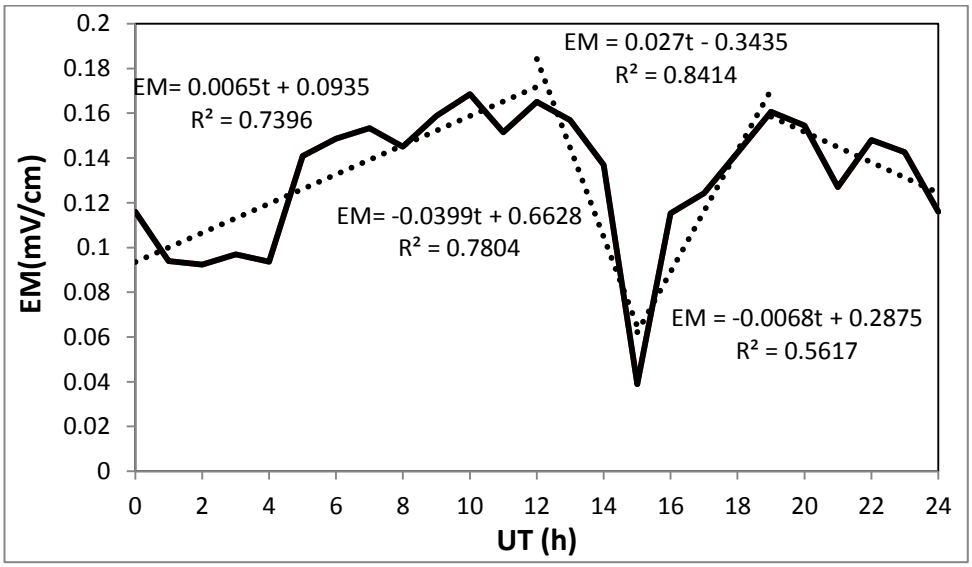

Figure 6. Magnetosphere convection electric field time variation for the one-day-shock activity.

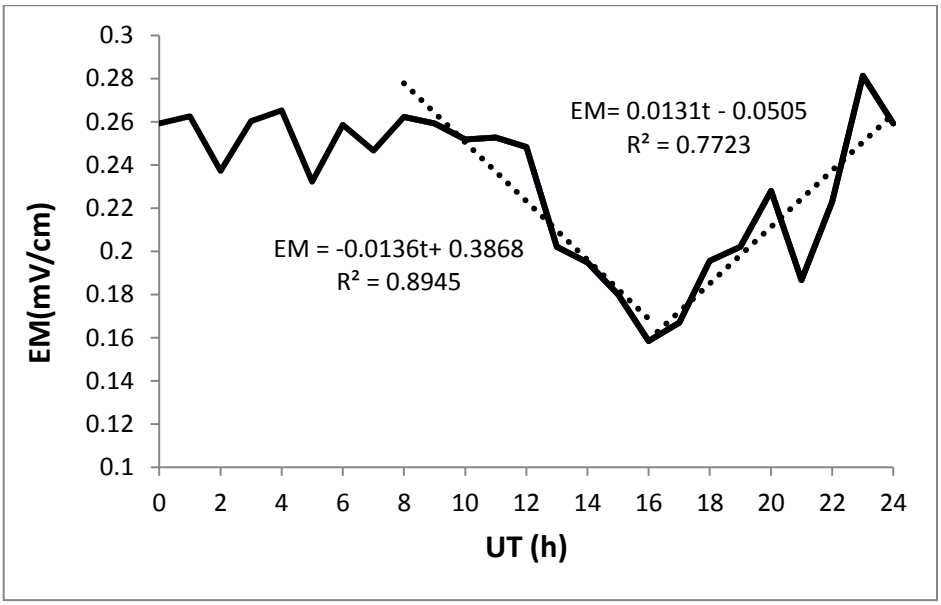

Figure 7. The same as figure 6 but for the two–days-shock activity.

seems to be non-sensitive to this type of shock until 1000 LT by exhibiting a fairly constant trend. The careful analysis of the graph points out that there are shortly successive time-changes (one hour) where the IMF turns from southward (increasing phase of the MCEF) to northward (decreasing phase of the MCEF). After that constant trend, the MCEF presents two trends. The decreasing phase of the MCEF following by the increasing one expresses that the IMF turns from northward to southward. Comparing the action of the one-day-shock and that of the two-days-shock, this remark reveals that added to the difference between the initial phase, another difference is observed during the last phase, the MECF of the one-day-shock activity is northward while that of the two-days-shock activity is southward.

The important conclusion that can be underlined is that it is impossible during two-days-shock period to assert that there is or not night side reconnection.

Figure 8 presents the diurnal variation of the MCEF

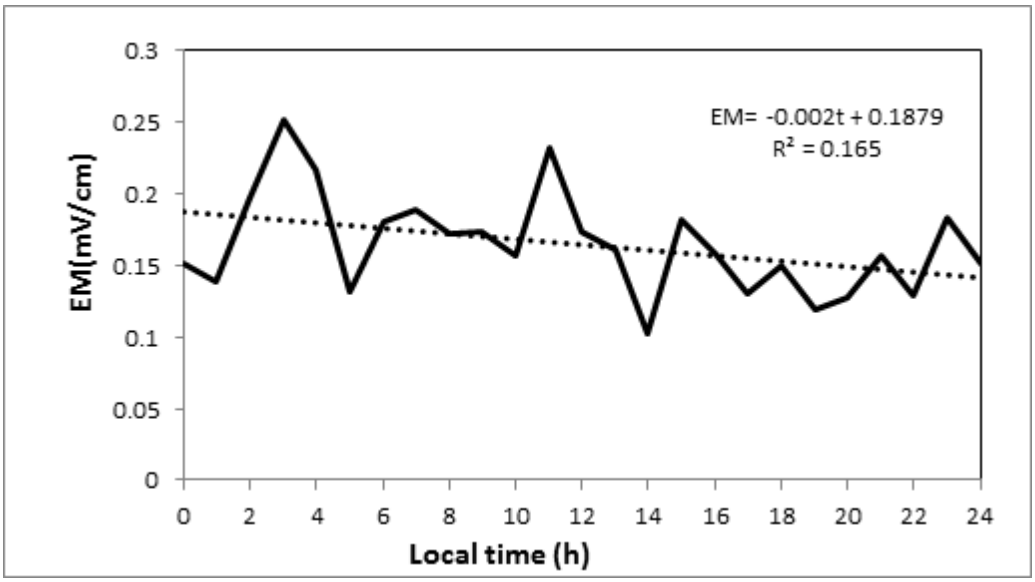

Figure 8. The same as figure 6 but for the three–days-shock activity.

during the three-days-shock activity. One can see the decreasing trend of the MCEF with a slope $-\frac{2\,10^{-3}mV}{cm.s}$ and 0.4062 as correlation coefficient value. The MCEF oscillates between its minimum value (0.101 mV/cm) and its maximum value (0.250 mV/cm) with a mean value of 0.250 mV/cm.

This type of shock is characteristic. In fact, the MCEF time variation shows the trend that characterizes a constant northward IMF due to the decreasing trend of the MCEF. But a careful analysis of the time profile of the MCEF during the three-days-shock activity shows that the IMF is always northward for the first and the last phases. We can assert here that there is no night side reconnection during the period of three-days-shock

Conclusion

The present work shows that the mean amplitudes of the MCEF during the whole disturbed period are inferior to those of the shock activity period. Moreover, during quiet time, the MCEF time profile presents a trough at 1400 LT and for the disturbed period at the same time we observe its maximum value.

It can be retained from this study that for the shock activity, the highest amplitudes of the MCEF are observed during the action of the two-days shock. The amplitudes vary from 0.158 to 0.281 mV/cm with a daily mean value of 0.229 mV/cm. The lowest amplitudes of the MCEF are produced by the one-day shock activity.

Whatever the type of shock, the MCEF intensity decreases from 1200 UT to 1400 UT and also between 2300 UT and 2400 UT. The trough is seen in the profile of the MCEF time variation between 1300 UT and 1700 UT during the shock activity where the minimums occur at 14 00 UT for the three-days-shock activity, at 1600 UT for the two-days-shock activity and at 1500 UT for the overall shock activity and for the one-day-shock activity.

The MCEF time profile during the whole disturbed activity and for the overall shock activity presents three trends (increasing, decreasing and increasing trends) beginning and ending by the southward IMF. The MCEF time profile of the one-day-shock shows four trends beginning by the southward IMF and ending by the northward IMF. The MCEF time profile of the two-days-shock is characterized by the non-sensitive change of the IMF followed by the signature of the northward IMF and finishing by that of the southward IMF. The MCEF of the three-days-shock is continuously decreased. This situation expresses the signature of the northward IMF.

It can be retained that: (1) it is better to treat separately on one hand each type of disturbed activity and on the other hand each type of shock. (2) the night reconnection does not occur during the one-day-shock and three-days-shock activities. For the whole shock activity and the two-days-shock activity it seems to be impossible to assert that there is or not a night time reconnection

CONFLICT OF INTERESTS

The authors have not declared any conflict of interests.

REFERENCES

Axford WI, Hines CO (1961). A unifying theory of high-latitude geophysical phenomena and geomagnetic storms. Canadian Journal of Physics 39:1433-1464.

de Siqueira PM, de Paula ER, Muella MTAH, Rezende LFC, Abdu MA,

Gonzalez WD (2011). Storm-time total electron contznt and its response to penetration electric fields over South America. Annales Geophysicae 29:1765-17778.
Dungey TW (1961). Interplanetary magnetic field and the auroral zones. Physical Review Letters 6(2):47-48.
Gnabahou DA, Ouattara F. (2012) Ionosphere Variability from 1957 to 1981 at Djibouti Station. European Journal of Scientific Research 73(3):382-390.
Gonzalez WD, Joselyn JA, Kamide Y, Kroehl HW, Rostoker G, Tsurutani BT, Vasyliunas VM. (1994). What is a geomagnetic storm? Journal of Geophysical Research 99(A4):5771-5792.
Kelley MC, Fejer BG, Gonzalez CA (1979). An explanation for anomalous ionospheric electric fields associated with northward turning of the interplanetary magnetic field. Geophysical Research Letters 6:301-304.
Gyébré AMF, Ouattara F, Kaboré S, Zerbo JL. (2015) Time variation of shock activity due to moderate and severe CMEs from 1966 to 1998. British Journal of Science 13(1):1-7.
Gyébré AMF, Gnabahou DA, Ouattara F (2018). The geomagnetic effects of solar activity as measured at Ouagadougou Station. International Journal of Astronomy and Astrophysics 8:178-190.
Legrand JP, Simon PA (1989). Solar Cycle and Geomagnetic Activity: A Review for Geophysicists. Part I. The Contributions to Geomagnetic Activity of Shock Waves and of the Solar Wind. Annals of Geophysics 7:565-578.
Mannucci AJ, Tsurutani BT, Abdu MA, Gonzalez WD, Komjathy A, Echer E, Iijima BA, Crowley G, Anderson D (2008). Superposed epoch analysis of the dayside ionospheric response to four intense geomagnetic storms. Journal of Geophysical Research 113:A00A02, doi:10.1029/2007JA012732
Mayaud PN (1971). A Measurement of Planetary Magnetic Activity Based on Two Antipodal Observatories. Annales Geophysicae 27:67-71.
Mayaud PN (1972). The aa Indices: A 100-Year Series, Characterizing the Magnetic Activity. Journal of Geophysical Research 77:6870-6874. http://dx.doi.org/10.1029/JA077i034p06870
McPherron RL, Weygand JM, Hsu TS (2007). Response of the Earth's magnetosphere to changes in the solar wind. Journal of Atmospheric and Solar-Terrestrial Physics Doi:10.1016/jastp.2007.08.040
Nishimura Y, Kikuchi T, Wygant J, Shinbori A, Ono T, Mtsuoka A, Nagatsuma T, Brautigam D (2009). Response of convection electric fields in the magnetosphere to IMF orientation change. Journal of Geophysical Research Vol. 114. A09206, 1-11. doi:10.1029/2009JA014277
Ouattara F, Amory Mazaudier C (2009) Solar-geomagnetic activity and Aa indices toward a standard classification. Journal of Atmospheric and Solar-Terrestrial Physics 71:1736-1748.
Partamies N, Juusola I, Tanskanen E, Kauristie K, Weygand JM, Ogawa Y (2011). Substorms during different phases. Annales Geophysicae 29:2011-2043.
Revah I, Bauer P (1982). Rapport d'activité du Centre de Recherches en Physique de l'environnement Terrestre et Planétaire, Note technique CRPE/115, 38-40 Rue du Général Leclerc 92131 Issy-Les Moulineaux.
Richardson IG, Cane HV. (2002) Sources of Geomagnetic Activity during Nearly Three Solar Cycles (1972- 2000). Journal of Geophysical Research 107:1187.
Richardson IG, Cliver EW, Cane HV (2000). Sources of Geomagnetic Activity over the Solar Cycle: Relative Importance of Coronal Mass Ejections, High-Speed Streams, and Slow Solar Wind. Journal of Geophysical Research 105:18200-18213. http://dx.doi.org/10.1029/1999JA000400
Russel CT (1979). The control of the magnetopause by the interplanetary magnetic fields. 3-21. In Dynamic of the magnetosphere. Akasofu S-I (ed.) University of Alaska, Geophysical Institute, Elvey CT Building, Fairbanks, Alaska, USA.
Russel CT (2007). The coupling of the solar wind to Earth's magnetosphere. In Space weather - Physics and effects. Volker Bothmer and Loannis A. Daglis (ed.) Springer, Praxis Publishing, Chichester, UK. pp. 103-130.
Simon PA, Legrand JP (1989). Solar Cycle and Geomagnetic Activity: A Review for Geophysicists. Part II. The Solar Sources of Geomagnetic Activity and Their Links with Sunspot Cycle Activity. Annals of Geophysics 7:579-594.
Tommaso A, Mirko P, Antonio V, Paula De M, Fabio L, Vincenzo C, Leonardo P (2016). Identification of the different magnetic field contributions during a geomagnetic storm in magnetospheric and ground observations. Annales Geophysicae 34:1069-1084
Zerbo JL, Ouattara F, Zoundi C, Gyébré AMF (2011). Cycle solaire 23 et activité géomagnétique depuis 1868. Révue CAMES-Série A, 12(2):255-262.

Related Journals: